

# Peak-structure in self-energy of cuprate superconductors

Yiqun Liu<sup>1\*</sup>, Yu Lan<sup>2\*</sup>, and Shiping Feng<sup>1†</sup>

<sup>1</sup>*Department of Physics, Beijing Normal University, Beijing 100875, China and*

<sup>2</sup>*College of Physics and Electronic Engineering, Hengyang Normal University, Hengyang 421002, China*

The recently deduced normal and anomalous self-energies from photoemission spectra of cuprate superconductors via the machine learning technique are calling for an explanation. Here the normal and anomalous self-energies in cuprate superconductors are analyzed within the framework of the kinetic-energy-driven superconductivity. It is shown that the exchanged spin excitations give rise to the well-pronounced low-energy peak-structures in both the normal and anomalous self-energies, however, they do not cancel in the total self-energy. In particular, the peak-structure in the normal self-energy is mainly responsible for the peak-dip-hump structure in the single-particle excitation spectrum, and can persist into the normal-state, while the sharp peak in the anomalous self-energy gives rise to a crucial contribution to the superconducting gap, and vanishes in the normal-state. Moreover, the evolution of the peak-structure with doping and momentum are also analyzed.

PACS numbers: 74.25.Jb, 74.20.Mn, 74.72.-h

## I. INTRODUCTION

The strong electron correlation is foundational to the emergence of superconductivity in cuprate superconductors<sup>1,2</sup>, where the strong interaction of the electrons with collective bosonic excitations of different origins results in (i) the energy and lifetime renormalization of the electrons in the particle-hole channel to form the quasiparticles responsible for the anomalous properties, and (ii) the formation of the electron pairs in the particle-particle channel responsible for superconductivity below the superconducting (SC) transition temperature  $T_c$ . This is why the quasiparticles in the SC-state determined by the electronic structure is intimately related to the pairing glue forming electron pairs<sup>3-7</sup>. In conventional superconductors, the renormalization of the electrons in the particle-hole channel and the formation of the electron pairs in the particle-particle channel are caused by the interaction between the electrons by the exchange of phonons<sup>8-10</sup>. Although a significant effort has been made for the past three decades, what type of the collective bosonic excitation that can mediate electron pairing in cuprate superconductors in analogy to the phonon-mediate pairing mechanism in conventional superconductors is still debated<sup>2-7</sup>.

Angle-resolved photoemission spectroscopy (ARPES) is a direct tool to probe the energy and momentum of quasiparticles simultaneously<sup>3-5</sup>, where a quasiparticle with a long lifetime is observed as a sharp peak in intensity, and a quasiparticle with a short lifetime is observed as a broad peak. However, the energy and lifetime of the quasiparticle in the SC-state are directly described by the real and imaginary parts of the total self-energy<sup>3-7</sup>  $\text{Re}\Sigma_{\text{tot}}(\mathbf{k}, \omega)$  and  $\text{Im}\Sigma_{\text{tot}}(\mathbf{k}, \omega)$ , respectively. This total self-energy  $\Sigma_{\text{tot}}(\mathbf{k}, \omega)$  is a specific combination

of the normal self-energy  $\Sigma_{\text{ph}}(\mathbf{k}, \omega)$  in the particle-hole channel and the anomalous self-energy  $\Sigma_{\text{pp}}(\mathbf{k}, \omega)$  in the particle-particle channel<sup>9-12</sup>. In other words, only the total self-energy can be extracted directly from ARPES experiments, and the only ingredient that needs to extract the total self-energy is the quasiparticle spectral density observed by ARPES experiments<sup>3-5</sup>. However, for our exploration of the bosonic mode coupling that is how electron self-energy effects appeared in our theoretical analysis, it is crucial to extract the normal and the anomalous self-energies separately<sup>9-12</sup>. This follows a basic fact that although both the normal and anomalous self-energies are generated by the same electron interaction mediated by collective bosonic excitations, they describe theoretically different parts of the interaction effects. The normal self-energy  $\Sigma_{\text{ph}}(\mathbf{k}, \omega)$  describes the single-particle coherence, and therefore competes with superconductivity. Moreover, it gives rise to a main contribution to the energy and lifetime renormalization of the electrons, and then all the anomalous properties of cuprate superconductors arise from this renormalization of the electrons<sup>13-16</sup>. On the other hand, the SC-state is characterized by the anomalous self-energy  $\Sigma_{\text{pp}}(\mathbf{k}, \omega)$ , which is identified as the energy and momentum dependent SC gap in the single-particle excitation spectrum, and therefore is corresponding to the energy for breaking an electron pair<sup>9-12</sup>. In this case, if both the normal and anomalous self-energies are deduced from the experimental data, it can be used to examine a microscopic SC theory and understand the details of the SC-state.

Although both the normal and anomalous self-energies can not be measured directly from ARPES experiments, the Boltzmann-machine learning technique<sup>17</sup> has been applied recently to deduce both the normal and anomalous self-energies from the experimental data of the ARPES spectra observed in  $\text{Bi}_2\text{Sr}_2\text{CaCu}_2\text{O}_{8+\delta}$  at the optimum doping and  $\text{Bi}_2\text{Sr}_2\text{CuO}_{6+\delta}$  in the underdoped regime<sup>18</sup>, and the deduced results show clearly that both the normal and anomalous self-energies exhibit the no-

<sup>†</sup>E-mail address: spfeng@bnu.edu.cn

\* These authors contributed equally to this work

table low-energy peak-structures, however, these low-energy peak-structures do not appear in the total self-energy. In particular, the peak in the anomalous self-energy makes a dominant contribution to the SC gap, and therefore provide a decisive testimony for the origin of superconductivity<sup>18</sup>. These normal and anomalous self-energies of cuprate superconductors revealed by the machine learning approach therefore are calling for a systematic analysis. Quite recently, these deduced normal and anomalous self-energies in Ref. 18 have been analyzed within an effective fermion-boson theory<sup>19</sup>, and the result indicates that the pairing electrons is mediated by a soft, near-critical bosonic mode. In particular, this analysis also shows that if the sharp low-energy peaks in both the normal and anomalous self-energies survive down to the lowest temperatures, their presence alone imposes the strong restrictions on the energy dependence of a soft pairing boson<sup>19</sup>. This conclusion is also similar to that obtained in terms of the machine learning approach<sup>18</sup>. However, the full understanding of these low-energy peak-structures in both normal and anomalous self-energies is still open for further analyses. In this paper, we make a comparison of the deduced normal and anomalous self-energies in Ref. 18 with those obtained based on the kinetic-energy-driven SC mechanism<sup>20–23</sup>, and then show explicitly that the interaction between electrons by the exchange of a strongly dispersive spin excitation generates the sharp low-energy peak-structures in both the normal and anomalous self-energies at around the antinodal region, which are in qualitative agreement with the corresponding results in both the normal and anomalous self-energies deduced via the machine learning technique<sup>18</sup>. However, these prominent low-energy peak-structures in both the normal and anomalous self-energies do not cancel in the total self-energy. Although the absence of this cancellation in the total self-energy is inconsistent with the corresponding result in the total self-energy deduced from the machine learning method<sup>18</sup>, it is well consistent with the corresponding experimental result in the total self-energy observed on cuprate superconductors<sup>24</sup>. Moreover, we show clearly that the sharp low-energy peak-structure in the normal self-energy is mainly responsible for the famous peak-dip-hump (PDH) structure in the single-particle excitation spectrum<sup>24–28</sup>, and can persist into the normal-state, while the sharp low-energy peak in the anomalous self-energy gives rise to a crucial contribution to the SC gap, and vanish in the normal-state.

In the remainder of this paper, the general formalism of the single-particle diagonal and off-diagonal propagators (then the normal and anomalous self-energies) obtained within the framework of the kinetic-energy-driven superconductivity is introduced briefly in Sec. II, while the quantitative characteristics of the normal and anomalous self-energies and the related exotic features of the electron quasiparticle excitations are presented in Sec. III, where we show that the sharp low-energy peak-structures in both the normal and anomalous self-energies are dop-

ing dependent. In particular, in the underdoped regime, the position of the peak in the anomalous self-energy at around the antinode moves further away from the Fermi energy with the increase of doping, while the peak in the normal self-energy at around the  $[\pi, 0]$  point of the Brillouin zone (BZ) moves towards to the Fermi energy. Furthermore, the sharp low-energy peak-structures also have a striking momentum dependence, with the position of the peak in the normal self-energy that shifts towards to the Fermi energy when one moves the momentum from the antinode to the node. Finally, we give a summary and discussions in Sec. IV.

## II. THEORETICAL FRAMEWORK

In cuprate superconductors, the single common feature in the layered crystal structure is the presence of the two-dimensional  $\text{CuO}_2$  planes<sup>1</sup>, and then it seems evident that the unconventional behaviors in cuprate superconductors are dominated by the strongly correlated motion of the electrons in these  $\text{CuO}_2$  planes. In this case, it has been suggested that the essential physics of the doped  $\text{CuO}_2$  plane can be properly accounted by the  $t$ - $J$  model on a square lattice<sup>2</sup>,

$$H = -t \sum_{\langle ll' \rangle_{\text{NN}\sigma}} C_{l\sigma}^\dagger C_{l'\sigma} + t' \sum_{\langle ll' \rangle_{\text{NNN}\sigma}} C_{l\sigma}^\dagger C_{l'\sigma} + \mu \sum_{l\sigma} C_{l\sigma}^\dagger C_{l\sigma} + J \sum_{\langle ll' \rangle_{\text{NN}}} \mathbf{S}_l \cdot \mathbf{S}_{l'}, \quad (1)$$

where we consider only the nearest-neighbor (NN) and next NN hopping terms, the summations  $\langle ll' \rangle_{\text{NN}}$  and  $\langle ll' \rangle_{\text{NNN}}$  denote that  $l$  runs over all sites, and for each  $l$ , over its NN sites and next NN sites, respectively,  $C_{l\sigma}^\dagger$  ( $C_{l\sigma}$ ) is the creation (annihilation) operator for an electron of spin  $\sigma$  on site  $l$ ,  $\mathbf{S}_l$  is a local spin operator, and  $\mu$  is the chemical potential. This  $t$ - $J$  model (1) is subject to an important on-site local constraint to avoid the double electron occupancy:  $\sum_{\sigma} C_{l\sigma}^\dagger C_{l\sigma} \leq 1$ . In order to satisfy this local constraint, we employ the charge-spin separation fermion-spin formalism<sup>22,29</sup>, in which the constrained electron operators  $C_{l\uparrow}$  and  $C_{l\downarrow}$  are replaced by,

$$C_{l\uparrow} = h_{l\uparrow}^\dagger S_l^-, \quad C_{l\downarrow} = h_{l\downarrow}^\dagger S_l^+, \quad (2)$$

respectively, where the spinful fermion operator  $h_{l\sigma} = e^{-i\Phi_{l\sigma}} h_l$  keeps track of the charge degree of freedom of the constrained electron together with some effects of spin configuration rearrangements due to the presence of the doped hole itself (charge carrier), while the spin operator  $S_l$  represents the spin degree of freedom of the constrained electron, and then the local constraint of no double occupancy is satisfied at each site in analytical calculations. In this fermion-spin representation (2), the

original  $t$ - $J$  model (1) can be rewritten as,

$$\begin{aligned}
H = & t \sum_{\langle ll' \rangle_{\text{NN}}} (h_{l'\uparrow}^\dagger h_{l\uparrow} S_l^+ S_{l'}^- + h_{l'\downarrow}^\dagger h_{l\downarrow} S_l^- S_{l'}^+) \\
& - t' \sum_{\langle ll' \rangle_{\text{NNN}}} (h_{l'\uparrow}^\dagger h_{l\uparrow} S_l^+ S_{l'}^- + h_{l'\downarrow}^\dagger h_{l\downarrow} S_l^- S_{l'}^+) \\
& - \mu \sum_{l\sigma} h_{l\sigma}^\dagger h_{l\sigma} + J_{\text{eff}} \sum_{\langle ll' \rangle_{\text{NN}}} \mathbf{S}_l \cdot \mathbf{S}_{l'}, \quad (3)
\end{aligned}$$

where  $S_l^- = S_l^x - iS_l^y$  and  $S_l^+ = S_l^x + iS_l^y$  are the spin-lowering and spin-raising operators for the spin  $S = 1/2$ , respectively,  $J_{\text{eff}} = (1 - \delta)^2 J$ , and  $\delta = \langle h_{l\sigma}^\dagger h_{l\sigma} \rangle$  is the charge-carrier doping concentration. Based on the  $t$ - $J$  model in this fermion-spin representation (3), the kinetic-energy-driven SC mechanism has been established<sup>20-23</sup>, where the interaction between the charge carriers directly from the kinetic energy of the  $t$ - $J$  model (3) by the exchange of a strongly dispersive *spin excitation* is responsible for the d-wave charge-carrier pairing in the particle-particle channel, then the d-wave electron pairs are due to the charge-spin recombination, and their condensation reveals the d-wave SC-state. The characteristic features of the kinetic-energy-driven SC mechanism can be summarized as<sup>20-23</sup>: (i) the mechanism is purely electronic without phonons; (ii) the mechanism indicates that the strong electron correlation favors superconductivity, since the main ingredient is identified into an electron pairing mechanism not involving the phonon, the external degree of freedom, but the internal spin degree of freedom of the constrained electron; (iii) the electron pairing state is controlled by both the electron pair gap and single-particle coherence, leading to that the maximal  $T_c$  occurs around the optimal doping, and then decreases in both the underdoped and the overdoped regimes. Within the framework of this kinetic-energy-driven superconductivity<sup>20-23</sup>, the renormalization of the electrons in cuprate superconductors has been investigated recently<sup>30-32</sup>, and the obtained main features of the single-particle excitation spectrum are well reproduced. The following analyses of the normal and anomalous self-energies in cuprate superconductors build on this kinetic-energy-driven SC mechanism<sup>20-23</sup>. In these previous works<sup>23</sup>, the single-particle diagonal and off-diagonal propagators of the  $t$ - $J$  model in the SC-state have been obtained in terms of the full charge-spin recombination, and can be expressed explicitly as,

$$G(\mathbf{k}, \omega) = \frac{1}{\omega - \varepsilon_{\mathbf{k}} - \Sigma_{\text{tot}}(\mathbf{k}, \omega)}, \quad (4a)$$

$$\mathfrak{S}^\dagger(\mathbf{k}, \omega) = \frac{L_{\mathbf{k}}(\omega)}{\omega - \varepsilon_{\mathbf{k}} - \Sigma_{\text{tot}}(\mathbf{k}, \omega)}, \quad (4b)$$

where the single-electron band energy  $\varepsilon_{\mathbf{k}} = -4t\gamma_{\mathbf{k}} + 4t'\gamma'_{\mathbf{k}} + \mu$ , with  $\gamma_{\mathbf{k}} = (\cos k_x + \cos k_y)/2$ ,  $\gamma'_{\mathbf{k}} = \cos k_x \cos k_y$ , and  $L_{\mathbf{k}}(\omega) = -\Sigma_{\text{pp}}(\mathbf{k}, \omega)/[\omega + \varepsilon_{\mathbf{k}} + \Sigma_{\text{ph}}(\mathbf{k}, -\omega)]$ , while the total self-energy  $\Sigma_{\text{tot}}(\mathbf{k}, \omega)$  is a well-known combination

of the normal self-energy  $\Sigma_{\text{ph}}(\mathbf{k}, \omega)$  and the anomalous self-energy  $\Sigma_{\text{pp}}(\mathbf{k}, \omega)$  as,

$$\Sigma_{\text{tot}}(\mathbf{k}, \omega) = \Sigma_{\text{ph}}(\mathbf{k}, \omega) + W_{\mathbf{k}}(\omega), \quad (5)$$

with the additional contribution  $W_{\mathbf{k}}(\omega)$  below  $T_c$  due to the SC gap opening,

$$W_{\mathbf{k}}(\omega) = \frac{|\Sigma_{\text{pp}}(\mathbf{k}, \omega)|^2}{\omega + \varepsilon_{\mathbf{k}} + \Sigma_{\text{ph}}(\mathbf{k}, -\omega)}. \quad (6)$$

In the framework of the kinetic-energy-driven superconductivity, both the normal and anomalous self-energies  $\Sigma_{\text{ph}}(\mathbf{k}, \omega)$  and  $\Sigma_{\text{pp}}(\mathbf{k}, \omega)$  arise from the interaction between electrons mediated by a strongly dispersive spin excitation, and have been derived explicitly in Ref. 23, where all order parameters and chemical potential are determined by the self-consistent calculation. In this sense, our calculation for both the normal and anomalous self-energies is controllable without using adjustable parameters. In particular, the sharp peak visible for temperature  $T \rightarrow 0$  in the normal (anomalous) self-energy is actually a  $\delta$ -functions, broadened by a small damping used in the numerical calculation at a finite lattice. The calculation in this paper for the normal (anomalous) self-energy is performed numerically on a  $160 \times 160$  lattice in momentum space, with the infinitesimal  $i0_+ \rightarrow i\Gamma$  replaced by a small damping  $\Gamma = 0.1J$ .

The single-particle spectral function  $A(\mathbf{k}, \omega)$  measured by ARPES experiments is related directly to the imaginary part of the single-particle diagonal propagator in Eq. (4a) as<sup>3-5</sup>,

$$A(\mathbf{k}, \omega) = \frac{-2\text{Im}\Sigma_{\text{tot}}(\mathbf{k}, \omega)}{[\omega - \varepsilon_{\mathbf{k}} - \text{Re}\Sigma_{\text{tot}}(\mathbf{k}, \omega)]^2 + [\text{Im}\Sigma_{\text{tot}}(\mathbf{k}, \omega)]^2}, \quad (7)$$

where  $\text{Re}\Sigma_{\text{tot}}(\mathbf{k}, \omega)$  and  $\text{Im}\Sigma_{\text{tot}}(\mathbf{k}, \omega)$  are the real and imaginary parts of the total self-energy  $\Sigma_{\text{tot}}(\mathbf{k}, \omega)$ , respectively. In ARPES experiments<sup>3-5</sup>, the energy renormalization of the electrons in cuprate superconductors is directly determined by the real part of the total self-energy, while the lifetime renormalization of the electrons is completely governed by the imaginary part of the total self-energy. This is also why only the total self-energy can be extracted directly from ARPES experiments. In the following discussions, the parameters in the  $t$ - $J$  model are chosen as  $t/J = 3.5$  and  $t'/t = 0.4$ . However, when necessary to compare with the experimental data, we take  $J = 100$  meV, which is the typical value of cuprate superconductors<sup>3-5</sup>.

### III. QUANTITATIVE CHARACTERISTICS

In an interacting electron system, the topology of the electron Fermi surface (EFS) plays a crucial role in the understanding of the physical properties, since everything happens near EFS. In particular, the strong coupling between the electrons and a strongly dispersive

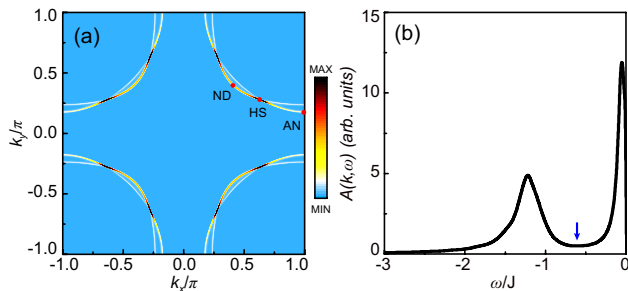


FIG. 1: (Color online) (a) The electron Fermi surface map and (b) the single-particle excitation spectrum at the antinode as a function of energy in  $\delta = 0.15$  with  $T = 0.002J$  for  $t/J = 3.5$  and  $t'/t = 0.4$ , where AN, HS, and ND in (a) denote the antinode, tip of the Fermi arc, and node, respectively, while the blue arrow in (b) indicates the position of the dip.

spin excitation in cuprate superconductors leads to a strong redistribution of the spectral weights on EFS<sup>30–32</sup>, which cause the normal and anomalous self-energies to strongly vary with the Fermi angle around EFS. For a convenience in the following discussions, (a) the underlying EFS map<sup>30</sup> and (b) the single-particle excitation spectrum<sup>30,31</sup>  $A(\mathbf{k}_{\text{AN}}, \omega)$  at the antinode as a function of energy for doping  $\delta = 0.15$  with temperature  $T = 0.002J$  are *replotted* in Fig. 1. The result in Fig. 1a therefore shows that EFS has been separated into three characteristic regions due to the strong redistribution of the spectral weight: (a) the antinodal region, where the spectral weight is suppressed, leading to that EFS around the antinodal region becomes unobservable in experiments<sup>33–36</sup>; (b) the nodal region, where the spectral weight is reduced modestly, leading to that EFS is truncated to form the disconnected Fermi arcs located around the nodal region<sup>33–36</sup>; (c) the region at around the tips of the Fermi arcs, where the renormalization from the quasiparticle scattering further reduces almost all spectral weight on Fermi arcs to the tips of the Fermi arcs<sup>37–40</sup>. In this case, the spectral intensity exhibits a largest value at around the tips of the Fermi arcs, where the characteristic feature is that both the real and imaginary parts of the normal self-energy have the anomalously small values<sup>30,31</sup>. In particular, the Fermi arcs collapse for the number of lattice sites  $N \rightarrow \infty$  at  $T \rightarrow 0$ , leading to form the Fermi-arc-tip liquid. Moreover, these tips of the Fermi arcs connected by the scattering wave vectors  $\mathbf{q}_i$  construct an *octet* scattering model, which is a basic scattering model in the explanation of the Fourier transform scanning tunneling spectroscopy (STS) experimental data, and also can give a consistent description of the regions of the highest joint density of states detected from ARPES autocorrelation experiments<sup>32,38</sup>. On the other hand, the result in Fig. 1b indicates that the characteristic feature in the single-particle excitation spectrum is the dramatic change in the spectral line-shape<sup>24–28</sup>, where a quasiparticle peak develops at the lowest energy, followed by a dip and a hump,

giving rise to a striking PDH structure. All these theoretical results are well consistent with the corresponding results observed from the ARPES experiments.

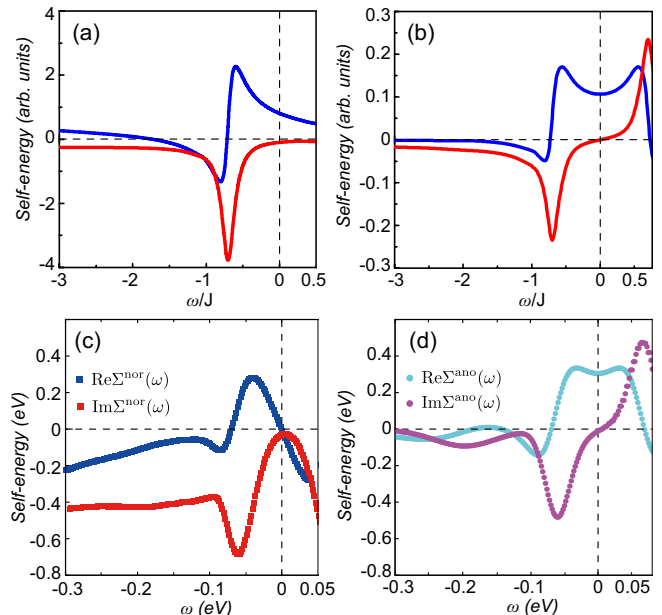


FIG. 2: (Color online) (a) The real (blue line) and imaginary (red line) parts of the normal self-energy and (b) the real (blue line) and imaginary (red line) parts of the anomalous self-energy at the antinode as a function of energy in  $\delta = 0.15$  with  $T = 0.002J$  for  $t/J = 3.5$  and  $t'/t = 0.4$ . The corresponding results of (c) the real and imaginary parts of the normal self-energy and (d) the real and imaginary parts of the anomalous self-energy around the antinode as a function of energy deduced from the ARPES spectra of the optimally doped  $\text{Bi}_2\text{Sr}_2\text{CaCu}_2\text{O}_{8+\delta}$  via the machine learning taken from Ref. 18.

We are now ready to analyze the doping and momentum dependence of the normal and anomalous self-energies in cuprate superconductors. In Fig. 2, we plot (a) the real (blue line) and imaginary (red line) parts of the normal self-energy and (b) the real (blue line) and imaginary (red line) parts of the anomalous self-energy at the antinode as a function of energy for  $\delta = 0.15$  with  $T = 0.002J$ . For a better comparison, the corresponding results<sup>18</sup> of (c) the real and imaginary parts of the normal self-energy and (d) the real and imaginary parts of the anomalous self-energy around the antinode as a function of energy deduced from the ARPES spectra of the optimally doped  $\text{Bi}_2\text{Sr}_2\text{CaCu}_2\text{O}_{8+\delta}$  via the machine learning technique are also shown in Fig. 2. Apparently, the main low-energy features of both the normal and anomalous self-energies deduced via the machine learning technique<sup>18</sup> are qualitatively reproduced, where all the real and imaginary parts of the normal and anomalous self-energies exhibit the prominent peak-structures in the low-energy region. Since the strength of the electron pair is directly determined by the anomalous self-energy, these peaks in both  $\text{Re}\Sigma_{\text{pp}}(\mathbf{k}_{\text{AN}}, \omega)$  and

$\text{Im}\Sigma_{\text{pp}}(\mathbf{k}_{\text{AN}}, \omega)$  give rise to a crucial contribution to the SC gap, and therefore are the true origin of the high  $T_c$  in cuprate superconductors<sup>18</sup>. On the other hand, since the single-particle coherence is associated directly with the normal self-energy, these peaks in  $\text{Re}\Sigma_{\text{ph}}(\mathbf{k}_{\text{AN}}, \omega)$  and  $\text{Im}\Sigma_{\text{ph}}(\mathbf{k}_{\text{AN}}, \omega)$  dominate the energy and lifetime renormalization of the electrons, respectively. In particular, the sharp change with energy in  $\text{Re}\Sigma_{\text{pp}}(\mathbf{k}_{\text{AN}}, \omega)$  and the large damping in  $\text{Im}\Sigma_{\text{pp}}(\mathbf{k}_{\text{AN}}, \omega)$  shown in Fig. 2b are also consistent with these results obtained in the very early numerical solution of the Eliashberg equations based on the spin-polaron  $t$ - $J$  model<sup>41</sup>, where the d-wave SC-state is mediated by the exchange of spin fluctuations. Moreover, it was shown<sup>42–46</sup> that the single-particle excitation spectra in the spin resonance mode mediated SC-state are close to those observed experimentally in cuprate superconductors, where both the normal and anomalous self-energies exhibit the sharp low-energy peak-structures<sup>42</sup>.

However, there is a substantial difference between theory and machine learning in the high-energy region, namely, the weaker features in the real and imaginary parts of the normal and anomalous self-energies occur in the high-energy region, while the calculation anticipates a flat featureless with the values of both the real and imaginary parts of the normal self-energy that approach zero. However, the actual range of the low-energy peak structures of the normal and anomalous self-energies is very similar in theory and machine learning. In particular, the sharp peak in  $\text{Im}\Sigma_{\text{pp}}(\mathbf{k}_{\text{AN}}, \omega)$  locates at the same energy  $\omega_{\text{Im-Th}} \sim -70$  meV as that in  $\text{Im}\Sigma_{\text{ph}}(\mathbf{k}_{\text{AN}}, \omega)$ , which has been confirmed by the deduced result of the normal (anomalous) self-energy based on the machine learning approach<sup>18</sup>. Moreover, this anticipated peak energy  $\omega_{\text{Im-Th}} \sim -70$  meV in the optimal doping is also qualitatively consistent with the corresponding result<sup>18</sup> of  $\omega_{\text{Im-ML}} \sim -65$  meV deduced in the optimally doped  $\text{Bi}_2\text{Sr}_2\text{CaCu}_2\text{O}_{8+\delta}$  via the machine learning technique.

In the SC-state, although the normal and anomalous self-energies describe theoretically different parts of the interaction effects, all of them make the contributions to the dramatic change in the spectral line-shape of the single-particle excitation spectrum. To see this point more clearly, we plot the imaginary part of the total self-energy  $\text{Im}\Sigma_{\text{tot}}(\mathbf{k}_{\text{AN}}, \omega)$  [then the quasiparticle scattering rate  $\Gamma(\mathbf{k}_{\text{AN}}, \omega) = -\text{Im}\Sigma_{\text{tot}}(\mathbf{k}_{\text{AN}}, \omega)$ ] at the antinode as a function of energy for  $\delta = 0.15$  with  $T = 0.002J$  in Fig. 3 in comparison with the corresponding ARPES experimental result<sup>24</sup> found in the optimally doped  $\text{Bi}_2\text{Sr}_2\text{CaCu}_2\text{O}_{8+\delta}$  around the antinode (inset). It should be noted that the sharp low-energy peak-structure in  $\text{Im}\Sigma_{\text{tot}}(\mathbf{k}_{\text{AN}}, \omega)$  in Fig. 3 is inconsistent with the corresponding result<sup>18</sup> deduced from the optimally doped  $\text{Bi}_2\text{Sr}_2\text{CaCu}_2\text{O}_{8+\delta}$  via the machine learning technique, where although the sharp low-energy peaks appear in both the normal and anomalous self-energies, they cancel in the imaginary part of the total self-energy to make the structure apparently invis-

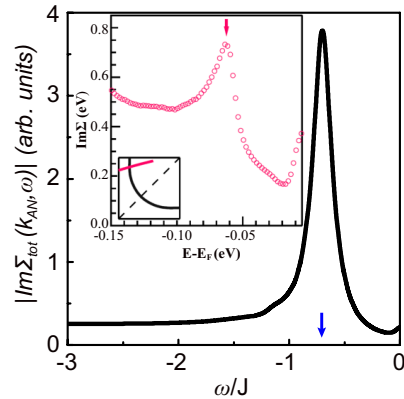


FIG. 3: (Color online) The imaginary part of the total self-energy at the antinode as a function of energy in  $\delta = 0.15$  with  $T = 0.002J$  for  $t/J = 3.5$  and  $t'/t = 0.4$ , where the blue arrow indicates the position of the peak. Inset: the corresponding experimental result of the optimally doped  $\text{Bi}_2\text{Sr}_2\text{CaCu}_2\text{O}_{8+\delta}$  taken from Ref. 24.

ble. However, this sharp low-energy peak-structure in  $\text{Im}\Sigma_{\text{tot}}(\mathbf{k}_{\text{AN}}, \omega)$  in Fig. 3 is very well consistent with the corresponding experimental result observed<sup>24</sup> in the optimally doped  $\text{Bi}_2\text{Sr}_2\text{CaCu}_2\text{O}_{8+\delta}$ . At the antinode,  $\text{Im}\Sigma_{\text{tot}}(\mathbf{k}_{\text{AN}}, \omega)$  reaches a sharp peak at the energy of  $-70$  meV, and then the weight of the peak decreases rapidly in both the low-energy and high-energy ranges. Concomitantly, this theoretical peak-energy of  $-70$  meV in the optimum doping is also in qualitative agreement with the peak energy<sup>24</sup> of  $-62$  meV detected in the optimally doped  $\text{Bi}_2\text{Sr}_2\text{CaCu}_2\text{O}_{8+\delta}$ . More surprisingly, the position of this sharp low-energy peak in  $\text{Im}\Sigma_{\text{tot}}(\mathbf{k}_{\text{AN}}, \omega)$  is just corresponding to the position of the dip in the PDH structure in the single-particle excitation spectrum shown in Fig. 1b, and therefore the sharp low-energy peak-structure in  $\text{Im}\Sigma_{\text{tot}}(\mathbf{k}_{\text{AN}}, \omega)$  induces an intensity depletion in the single-particle excitation spectrum around the dip<sup>31</sup>. The physical origin of this intensity depletion around the dip in the PDH structure [then the sharp low-energy peak-structure in  $\text{Im}\Sigma_{\text{tot}}(\mathbf{k}, \omega)$ ] can be attributed to the emergence of the momentum dependence of the pseudogap. This follows a fact that the normal self-energy  $\Sigma_{\text{ph}}(\mathbf{k}, \omega)$  in Eq. (4) can be also rewritten as<sup>23</sup>,

$$\Sigma_{\text{ph}}(\mathbf{k}, \omega) \approx \frac{[\bar{\Delta}_{\text{PG}}(\mathbf{k})]^2}{\omega + \varepsilon_{0\mathbf{k}}}, \quad (8)$$

where the corresponding energy spectrum  $\varepsilon_{0\mathbf{k}}$  and the pseudogap  $\bar{\Delta}_{\text{PG}}(\mathbf{k})$  are derived directly from the normal self-energy  $\Sigma_{\text{ph}}(\mathbf{k}, \omega)$  and its antisymmetric part  $\Sigma_{\text{pho}}(\mathbf{k}, \omega)$  as  $\varepsilon_{0\mathbf{k}} = -\Sigma_{\text{ph}}(\mathbf{k}, 0)/\Sigma_{\text{pho}}(\mathbf{k}, 0)$  and  $\bar{\Delta}_{\text{PG}}(\mathbf{k}) = \Sigma_{\text{ph}}(\mathbf{k}, 0)/\sqrt{-\Sigma_{\text{pho}}(\mathbf{k}, 0)}$ , respectively, and have been given explicitly in Ref. 23. This pseudogap  $\bar{\Delta}_{\text{PG}}(\mathbf{k})$  is therefore identified as being a region of the electron self-energy effect by which it means the spectral intensity is suppressed. In particular, the result in Eq. (8) also indicates that the imaginary part of the total self-energy  $\text{Im}\Sigma_{\text{tot}}(\mathbf{k}, \omega) \propto \text{Im}\Sigma_{\text{ph}}(\mathbf{k}, \omega) \approx 2\pi[\bar{\Delta}_{\text{PG}}(\mathbf{k})]^2\delta(\omega +$

$\varepsilon_{0\mathbf{k}}$ ), and then the pseudogap  $\bar{\Delta}_{\text{PG}}(\mathbf{k})$  plays the same role in the inducement of an intensity depletion in the single-particle excitation spectrum around the dip as that of  $\text{Im}\Sigma_{\text{tot}}(\mathbf{k}, \omega)$ . In other words, the pseudogap-induced low-energy peak-structure in  $\text{Im}\Sigma_{\text{tot}}(\mathbf{k}, \omega)$  [then  $\bar{\Delta}_{\text{PG}}(\mathbf{k})$ ] in Fig. 3 is directly responsible for the famous PDH structure in the single-particle excitation spectrum shown in Fig. 1b. Moreover, since  $\text{Im}\Sigma_{\text{tot}}(\mathbf{k}, \omega) \propto \text{Im}\Sigma_{\text{ph}}(\mathbf{k}, \omega) \sim [\bar{\Delta}_{\text{PG}}(\mathbf{k})]^2$ , the appearance of the sharp low-energy peak-structure in  $\text{Im}\Sigma_{\text{tot}}(\mathbf{k}, \omega)$  is determined mainly by  $\text{Im}\Sigma_{\text{ph}}(\mathbf{k}, \omega)$  [then  $\bar{\Delta}_{\text{PG}}(\mathbf{k})$ ], reflecting a basic fact that the main feature of the pseudogap-induced low-energy peak-structure in  $\text{Im}\Sigma_{\text{tot}}(\mathbf{k}_{\text{AN}}, \omega)$  can persist into the normal-state<sup>31</sup>, leading to that the PDH structure is totally unrelated to superconductivity.

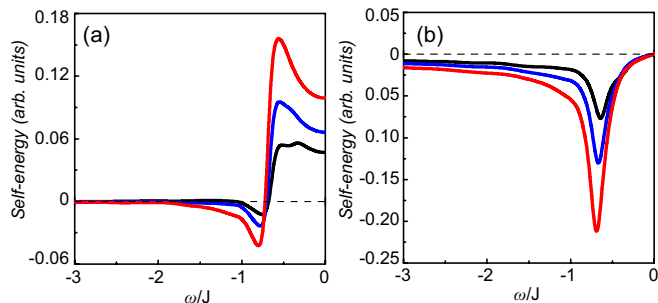


FIG. 4: (Color online) The (a) real and (b) imaginary parts of the anomalous self-energy at the antinode as a function of energy in  $\delta = 0.06$  (black line),  $\delta = 0.09$  (blue line), and  $\delta = 0.12$  (red line) with  $T = 0.002J$  for  $t/J = 3.5$  and  $t'/t = 0.4$ .

As a natural consequence of the doped Mott insulators, the normal and anomalous self energies in cuprate superconductors evolve with doping. In Fig. 4, we plot the results of the (a) real and (b) imaginary parts of the anomalous self-energy at the antinode as a function of energy for  $\delta = 0.06$  (black line),  $\delta = 0.09$  (blue line), and  $\delta = 0.12$  (red line) with  $T = 0.002J$ . It is thus shown clearly that in the underdoped regime, when the doping concentration is increased, (i) the low-energy peaks in both  $\text{Re}\Sigma_{\text{pp}}(\mathbf{k}_{\text{AN}}, \omega)$  and  $\text{Im}\Sigma_{\text{pp}}(\mathbf{k}_{\text{AN}}, \omega)$  move further away from the Fermi energy, and (ii) the weights of these low-energy peaks are increased, which are nothing, but the SC gap that increases in magnitude with doping in the underdoped regime. Moreover, the evolution of the imaginary part of the normal self-energy with doping at around the  $[\pi, 0]$  point of BZ has been also investigated<sup>31</sup>, and results show that in the underdoped regime, the low-energy peak in  $\text{Im}\Sigma_{\text{ph}}(\mathbf{k}, \omega)|_{\mathbf{k}=[\pi, 0]}$  shifts further towards to the Fermi energy with the increase of doping, which leads to that both the hump and lowest-energy peak in the PDH structure of the single-particle excitation spectrum at around the  $[\pi, 0]$  point move further towards to the Fermi energy with the increase of doping, also in qualitative agreement with the corresponding ARPES experimental results<sup>27</sup>.

Now we turn to discuss the evolution of the normal and anomalous self-energies with momentum. In Fig.

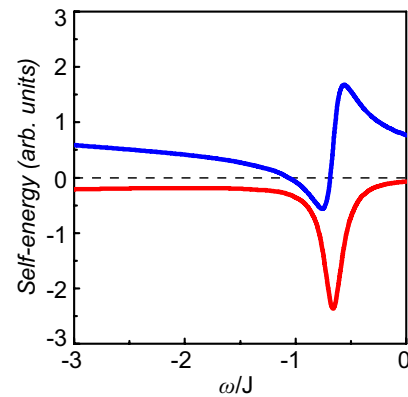


FIG. 5: (Color online) The real (blue line) and imaginary (red line) parts of the normal self-energy at the node as a function of energy in  $\delta = 0.15$  with  $T = 0.002J$  for  $t/J = 3.5$  and  $t'/t = 0.4$ .

5, we plot the real (blue line) and imaginary (red line) parts of the normal self-energy at the node as a function of energy for  $\delta = 0.15$  with  $T = 0.002J$ . In comparison with the corresponding result in Fig. 2a for the same set of parameters except for at the node, it is shown clearly when one moves the momentum  $\mathbf{k}_{\text{F}}$  from the antinode to the node, the weights of the low-energy peaks in both  $\text{Re}\Sigma_{\text{ph}}(\mathbf{k}_{\text{ND}}, \omega)$  and  $\text{Im}\Sigma_{\text{ph}}(\mathbf{k}_{\text{ND}}, \omega)$  are reduced, while the low-energy peaks move further towards to the Fermi energy. On the other hand, in the kinetic-energy-driven SC mechanism<sup>20-23</sup>, the characteristic feature of the d-wave SC-state is the existence of four nodes on EFS, where the SC gap vanishes  $\Sigma_{\text{pp}}(\mathbf{k}_{\text{ND}}, \omega) = 0$ . Moreover, it has been found in the previous studies that the low-energy peak structures in both the normal and anomalous self-energies disappear at around the tips of the Fermi arcs<sup>30-32</sup>, where  $\Sigma_{\text{ph}}(\mathbf{k}_{\text{HS}}, \omega)$  and  $\Sigma_{\text{pp}}(\mathbf{k}_{\text{HS}}, \omega)$  have the anomalously small values, reflecting a fact that the coupling strength of the electrons to a strongly dispersive spin excitation is quite weak<sup>47</sup>. Concomitantly, the imaginary part of the total self-energy  $\text{Im}\Sigma_{\text{tot}}(\mathbf{k}_{\text{HS}}, \omega)$  has an anomalously small value at around the tips of the Fermi arcs<sup>30-32</sup>, which has been confirmed by the experiments<sup>37-40</sup>, where the weakest quasiparticle scattering that occurs at around the tips of the Fermi arcs has been observed. This is also why the spectral intensity exhibits a largest value at around the tips of the Fermi arcs shown in Fig. 1.

At the temperature above  $T_c$ , the electrons are in a normal-state, where the SC gap  $\Sigma_{\text{pp}}(\mathbf{k}, \omega) = 0$ . However, the low-energy peak-structure in the normal self-energy can persist into the normal-state. To see this point more clearly, we plot the results of the real (blue line) and imaginary (red line) parts of the normal self-energy at (a) the antinode and (b) the node as a function of energy for  $\delta = 0.15$  with  $T = 0.15J$  in Fig. 6. In comparison with the corresponding results in Fig. 2a and Fig. 5 for the same set of parameters except for in the normal-state



( $T = 0.15J$ ), one can find that although the weights of the low-energy peaks are suppressed with the increase of temperatures, the positions of these low-energy peaks in the normal-state do not change much from the corresponding case in the SC-state. This is why some characteristic features in the single-particle excitation spectrum of cuprate superconductors arising from the renormalization of the electrons can be detected from experiments in both the SC-state and normal-state.

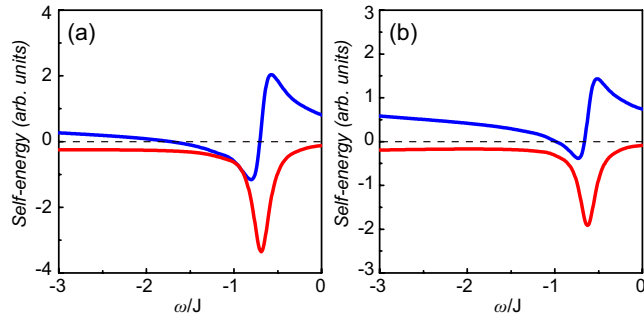


FIG. 6: (Color online) The real (blue line) and imaginary (red line) parts of the normal self-energy at (a) the antinode and (b) the node as a function of energy in  $\delta = 0.15$  with  $T = 0.15J$  for  $t/J = 3.5$  and  $t'/t = 0.4$ .

As we have mentioned above in Sec. II, one of the characteristic features in the kinetic-energy-driven SC mechanism is that the SC-state is controlled by both the electron pair gap and single-particle coherence. In this case, to examine the microscopic theory of the kinetic-energy-driven superconductivity, it need to compare the obtained normal and anomalous self-energies with the corresponding results deduced via the machine learning method, and the obtained total self-energy with the corresponding experimental data. Our present study shows that in the kinetic-energy-driven superconductivity, the exchanged spin excitations give rise to the low-energy peak-structures in both the normal self-energy  $\Sigma_{\text{ph}}(\mathbf{k}, \omega)$  and anomalous self-energy  $\Sigma_{\text{pp}}(\mathbf{k}, \omega)$ , which are in qualitative agreement with the corresponding low-energy peak-structures in both the normal and anomalous self-energies deduced from the ARPES spectra of cuprate superconductors via the machine learning technique<sup>18</sup>. Concomitantly, these low-energy peak-structures in both the normal and anomalous self-energies do not cancel in the total self-energy, and then the well-pronounced low-energy peak-structure also appears in the total self-energy  $\Sigma_{\text{tot}}(\mathbf{k}, \omega)$ , which is well consistent with the corresponding low-energy peak-structure in the total self-energy observed experimentally on cuprate superconductors<sup>24</sup>. The qualitative agreement between the low-energy peak-structures in both the normal and anomalous self-energies obtained based on the kinetic-energy-driven superconductivity and those deduced from the ARPES spectra of cuprate superconductors via the machine learning technique<sup>18</sup> together with the good agreement between theory and

experiment<sup>24</sup> for the low-energy peak-structure in the total self-energy therefore shows why the theory of the kinetic-energy-driven superconductivity can give a consistent description of the renormalization of the electrons in cuprate superconductors<sup>30–32</sup>.

In the machine learning analysis in Ref. 18, the low-energy peak-structures in both the hidden normal and anomalous self-energies of cuprate superconductors are deduced solely from the complicated ARPES line-shape, which therefore provide a fingerprint of the SC mechanism. However, within the present machine learning method<sup>18</sup>, the deduced cancellation effect of these low-energy peaks in the total self-energy making the structure apparently invisible is inconsistent with the corresponding experimental observations<sup>24</sup>, where the notable low-energy peak-structure in the total self-energy has been observed experimentally. On the other hand, the strong coupling of the electrons with a strongly dispersive spin excitation in cuprate superconductors induces a strong EFS reconstruction, which complicate the low-energy electronic state properties. Our present study therefore call for a systematic analysis with the improvements in the machine learning method to obtain the more accurate results of the hidden quantities, including the normal and anomalous self-energies, at all around EFS from the experimental data observed from the ARPES measurements with the improved resolution, together with other powerful measurement techniques, such as STS, Raman scattering, and infrared measurements of the reflectance. These more accurate results of the hidden quantities would be crucial to the understanding of the essential physics of cuprate superconductors and the related kinetic-energy-driven SC mechanism.

#### IV. CONCLUSIONS

In summary, we have compared the results of the normal and anomalous self-energies deduced from the ARPES spectra of cuprate superconductors via the machine learning technique with these obtained based on the kinetic-energy-driven superconductivity, and the obtained results show that both the normal and anomalous self-energies due to the interaction between electrons mediated by a strongly dispersive spin excitation exhibit the notable low-energy peak-structures at all around EFS except for at the tips of the Fermi arcs, where the low-energy peak-structures are predicted to be absent<sup>30–32</sup>. However, these prominent low-energy peak-structures in both the normal and anomalous self-energies do not cancel in the total self-energy, leading to the appearance of the low-energy peak-structure in the total self-energy. In particular, the low-energy peak-structure in the normal self-energy is mainly responsible for the PDH structure in the single-particle excitation spectrum, and can persist into the normal-state, while the low-energy peak in the anomalous self-energy gives rise to a crucial contribution to the SC gap, and vanishes in the normal-state.

Furthermore, these low-energy peak-structures in both the normal and anomalous self-energies evolve with doping, where the low-energy peak in the anomalous self-energy at around the antinode region moves further away from the Fermi energy as the doping concentration is increased in the underdoped regime. More specifically, these low-energy peaks have a special momentum dependence, where although the weight of the low-energy peak in the normal self-energy is gradually reduced when one moves the momentum from antinode to node, the position of the low-energy peak moves towards to the Fermi

energy.

### Acknowledgements

This work was supported by the National Key Research and Development Program of China under Grant No. 2016YFA0300304, and the National Natural Science Foundation of China under Grant Nos. 11974051 and 11734002.

- 
- <sup>1</sup> J. G. Bednorz and K. A. Müller, *Z. Phys. B* **64**, 189 (1986).  
<sup>2</sup> P. W. Anderson, *Science* **235**, 1196 (1987).  
<sup>3</sup> See, e.g., the review, A. Damascelli, Z. Hussain, and Z.-X. Shen, *Rev. Mod. Phys.* **75**, 473 (2003).  
<sup>4</sup> See, e.g., the review, J. C. Campuzano, M. R. Norman, M. Randeria, in *Physics of Superconductors*, vol. II, edited by K. H. Bennemann and J. B. Ketterson (Springer, Berlin Heidelberg New York, 2004), p. 167.  
<sup>5</sup> See, e.g., the review, Joerg Fink, Sergey Borisenko, Alexander Kordyuk, Andreas Koitzsch, Jochen Geck, Volodymyr Zabalotnyy, Martin Knupfer, Bernd Buechner, and Helmut Berger, in *Lecture Notes in Physics*, vol. 715, edited by Stefan Hüfner (Springer-Verlag Berlin Heidelberg, 2007), p. 295.  
<sup>6</sup> See, e.g., the review, Jules P. Carbotte, Thomas Timusk, and Jungseok Hwang, *Rep. Prog. Phys.* **74**, 066501 (2011).  
<sup>7</sup> Jin Mo Bok, Jong Ju Bae, Han-Yong Choi, Chandra M. Varma, W. Zhang, J. He, Y. Zhang, L. Yu, and X. J. Zhou, *Sci. Adv.* **2**, e1501329 (2016).  
<sup>8</sup> J. Bardeen, L. N. Cooper, and J. R. Schrieffer, *Phys. Rev.* **108**, 1175 (1957).  
<sup>9</sup> G. M. Eliashberg, *Sov. Phys. JETP* **11**, 696 (1960).  
<sup>10</sup> D. J. Scalapino, J. R. Schrieffer, and J. W. Wilkins, *Phys. Rev.* **148**, 263 (1966).  
<sup>11</sup> L. P. Gorkov, *Sov. Phys. JETP* **34**, 505 (1958).  
<sup>12</sup> Y. Nambu, *Phys. Rev.* **117**, 648 (1960).  
<sup>13</sup> See, e.g., the review, Tom Timusk and Bryan Statt, *Rep. Prog. Phys.* **62**, 61 (1999).  
<sup>14</sup> See, e.g., the review, S. Hüfner, M. A. Hossain, A. Damascelli, and G. A. Sawatzky, *Rep. Prog. Phys.* **71**, 062501 (2008).  
<sup>15</sup> See, e.g., the review, Riccardo Comin and Andrea Damascelli, *Annu. Rev. Condens. Matter Phys.* **7**, 369 (2016).  
<sup>16</sup> See, e.g., the review, I. M. Vishik, *Rep. Prog. Phys.* **81**, 062501 (2018).  
<sup>17</sup> D. H. Ackley, G. E. Hinton, T. J. Sejnowski, *Cognitive Science* **9**, 147 (1985); P. Smolensky, in *Parallel Distributed Processing*, vol. 1, edited by D. E. Rumelhart and J. L. McClelland (MIT Press, Cambridge, 1986), pp. 194-281.  
<sup>18</sup> Youhei Yamaji, Teppei Yoshida, Atsushi Fujimori, and Masatoshi Imada, arXiv:1903.08060.  
<sup>19</sup> Andrey V. Chubukov and Jörg Schmalian, *Phys. Rev. B* **101**, 180510(R) (2020).  
<sup>20</sup> Shiping Feng, *Phys. Rev. B* **68**, 184501 (2003); Shiping Feng, Tianxing Ma, and Huaiming Guo, *Physica C* **436**, 14 (2006).  
<sup>21</sup> Shiping Feng, Huaisong Zhao, and Zheyu Huang, *Phys. Rev. B* **85**, 054509 (2012); *Phys. Rev. B* **85**, 099902(E) (2012).  
<sup>22</sup> See, e.g., the review, Shiping Feng, Yu Lan, Huaisong Zhao, Lülin Kuang, Ling Qin, and Xixiao Ma, *Int. J. Mod. Phys. B* **29**, 1530009 (2015).  
<sup>23</sup> Shiping Feng, Lülin Kuang, and Huaisong Zhao, *Physica C* **517**, 5 (2015).  
<sup>24</sup> Daixiang Mou, Adam Kaminski, and Genda Gu, *Phys. Rev. B* **95**, 174501 (2017).  
<sup>25</sup> D. S. Dessau, B. O. Wells, Z.-X. Shen, W. E. Spicer, A. J. Arko, R. S. List, D. B. Mitzi, and A. Kapitulnik, *Phys. Rev. Lett.* **66**, 2160 (1991).  
<sup>26</sup> M. R. Norman, H. Ding, J. C. Campuzano, T. Takeuchi, M. Randeria, T. Yokoya, T. Takahashi, T. Mochiku, and K. Kadowaki, *Phys. Rev. Lett.* **79**, 3506 (1997).  
<sup>27</sup> J. C. Campuzano, H. Ding, M. R. Norman, H. M. Fretwell, M. Randeria, A. Kaminski, J. Mesot, T. Takeuchi, T. Sato, T. Yokoya, T. Takahashi, T. Mochiku, K. Kadowaki, P. Guptasarma, D. G. Hinks, Z. Konstantinovic, Z. Z. Li, and H. Raffy, *Phys. Rev. Lett.* **83**, 3709 (1999).  
<sup>28</sup> J. Wei, Y. Zhang, H. W. Ou, B. P. Xie, D. W. Shen, J. F. Zhao, L. X. Yang, M. Arita, K. Shimada, H. Namatame, M. Taniguchi, Y. Yoshida, H. Eisaki, and D. L. Feng, *Phys. Rev. Lett.* **101**, 097005 (2008).  
<sup>29</sup> Shiping Feng, Jihong Qin, and Tianxing Ma, *J. Phys.: Condens. Matter* **16**, 343 (2004); Shiping Feng, Z. B. Su, and L. Yu, *Phys. Rev. B* **49**, 2368 (1994).  
<sup>30</sup> Deheng Gao, Yiqun Liu, Huaisong Zhao, Yingping Mou, and Shiping Feng, *Physica C* **551**, 72 (2018); Yiqun Liu, Yu Lan, Yingping Mou, and Shiping Feng, *Physica C* **576**, 1353661 (2020).  
<sup>31</sup> Deheng Gao, Yingping Mou, and Shiping Feng, *J. Low Temp. Phys.* **192**, 19 (2018); Shiping Feng, Deheng Gao, Yiqun Liu, Yingping Mou, and Shuning Tan, *J. Supercond. Nov. Magn.* **32**, 2745 (2019).  
<sup>32</sup> Deheng Gao, Yingping Mou, Yiqun Liu, Shuning Tan, and Shiping Feng, *Phil. Mag.* **99**, 752 (2019).  
<sup>33</sup> M. R. Norman, H. Ding, M. Randeria, J. C. Campuzano, T. Yokoya, T. Takeuchi, T. Takahashi, T. Mochiku, K. Kadowaki, P. Guptasarma, and D. G. Hinks, *Nature* **392**, 157 (1998).  
<sup>34</sup> A. Kanigel, M. R. Norman, M. Randeria, U. Chatterjee, S. Souma, A. Kaminski, H. M. Fretwell, S. Rosenkranz, M. Shi, T. Sato, T. Takahashi, Z. Z. Li, H. Raffy, K. Kadowaki, D. Hinks, L. Ozyuzer, and J. C. Campuzano, *Nature Phys.* **2**, 447 (2006).  
<sup>35</sup> T. Yoshida, X. J. Zhou, K. Tanaka, W. L. Yang, Z. Hus-



- sain, Z.-X. Shen, A. Fujimori, S. Sahrakorpi, M. Lindroos, R. S. Markiewicz, A. Bansil, Seiki Komiy, Yoichi Ando, H. Eisaki, T. Kakeshita, and S. Uchida, *Phys. Rev. B* **74**, 224510 (2006).
- <sup>36</sup> Takeshi Kondo, Ari D. Palczewski, Yoichiro Hamaya, Tsunehiro Takeuchi, J. S. Wen, Z. J. Xu, Genda Gu, and Adam Kaminski, *Phys. Rev. Lett.* **111**, 157003 (2013).
- <sup>37</sup> B. Loret, Y. Gallais, M. Cazayous, R. D. Zhong, J. Schneeloch, G. D. Gu, A. Fedorov, T. K. Kim, S. V. Borisenko, and A. Sacuto, *Phys. Rev. B* **97**, 174521 (2018).
- <sup>38</sup> U. Chatterjee, M. Shi, A. Kaminski, A. Kanigel, H. M. Fretwell, K. Terashima, T. Takahashi, S. Rosenkranz, Z. Z. Li, H. Raffy, A. Santander-Syro, K. Kadowaki, M. R. Norman, M. Randeria, and J. C. Campuzano, *Phys. Rev. Lett.* **96**, 107006 (2006).
- <sup>39</sup> Yang He, Yi Yin, M. Zech, Anjan Soumyanarayanan, Michael M. Yee, Tess Williams, M. C. Boyer, Kamallesh Chatterjee, W. D. Wise, I. Zeljkovic, Takeshi Kondo, T. Takeuchi, H. Ikuta, Peter Mistark, Robert S. Markiewicz, Arun Bansil, Subir Sachdev, E. W. Hudson, and J. E. Hoffman, *Science* **344**, 608 (2014).
- <sup>40</sup> Y. Sassa, M. Radović, M. Månsson, E. Razzoli, X. Y. Cui, S. Pailhès, S. Guerrero, M. Shi, P. R. Willmott, F. Miletto Granozio, J. Mesot, M. R. Norman and L. Patthey, *Phys. Rev. B* **83**, 140511(R) (2011).
- <sup>41</sup> N. M. Plakida, V. S. Oudovenko, P. Horsch, and A. I. Liechtenstein, *Phys. Rev. B* **55**, R11997 (1997).
- <sup>42</sup> F. Onufrieva and P. Pfeuty, *Phys. Rev. Lett.* **102**, 207003 (2009).
- <sup>43</sup> P. Monthoux and D. Pines, *Phys. Rev. Lett.* **69**, 961 (1992).
- <sup>44</sup> F. Onufrieva and P. Pfeuty, *Phys. Rev. B* **65**, 054515 (2002).
- <sup>45</sup> S. S. Kancharla, B. Kyung, D. Sénéchal, M. Civelli, M. Capone, G. Kotliar, and A.-M. S. Tremblay, *Phys. Rev. B* **77**, 184516 (2008); O. Simard, C.-D. Hébert, A. Foley, D. Sénéchal, and A.-M. S. Tremblay *Phys. Rev. B* **100**, 094506 (2019).
- <sup>46</sup> F. Onufrieva and P. Pfeuty, *Phys. Rev. Lett.* **109**, 257001 (2012); J. Vučićević, T. Ayrar, and O. Parcollet, *Phys. Rev. B* **96**, 104504 (2017).
- <sup>47</sup> Yingping Mou, Yiqun Liu, Shuning Tan, and Shiping Feng, *Phil. Mag.* **99**, 2718 (2019).